Check for updates

AGU ADVANCING EARTH AND SPACE SCIENCE

Geophysical Research Letters®

RESEARCH LETTER
10.1029/2022GL102105

Unprecedented Winter Rainfall Initiates Large Snow Avalanche and Mass Movement Cycle in New Zealand's Southern Alps/Kā Tiritiri o te Moana

Aubrey D. Miller[1], Todd A. N. Redpath[1,2], Pascal Sirguey[1], Simon C. Cox[3], Perry Bartelt[4,5], Don Bogie[6], Jono P. Conway[7], Nicolas J. Cullen[2], and Yves Bühler[4,5]

[1]National School of Surveying, University of Otago, Dunedin, New Zealand, [2]School of Geography, University of Otago, Dunedin, New Zealand, [3]GNS Science, Dunedin, New Zealand, [4]WSL Institute for Snow and Avalanche Research SLF, Davos Dorf, Switzerland, [5]Climate Change, Extremes and Natural Hazards in Alpine Regions Research Center CERC, Davos Dorf, Switzerland, [6]Department of Conservation, Christchurch, New Zealand, [7]National Institute of Water & Atmospheric Research, Lauder, New Zealand

Key Points:

- Record-breaking winter storm bringing rain to high elevations triggered a series of alpine mass movements in New Zealand's Southern Alps
- Snow avalanches were successfully diverted away from Aoraki/Mount Cook Village in the largest avalanche cycle observed in decades
- Event documentation and modeling help anticipate future hazards for such rain-on-snow induced mass movements on deep mid-winter snowpacks

Supporting Information:

Supporting Information may be found in the online version of this article.

Correspondence to:

A. D. Miller,
aubrey.miller@otago.ac.nz

Citation:

Miller, A. D., Redpath, T. A. N., Sirguey, P., Cox, S. C., Bartelt, P., Bogie, D., et al. (2023). Unprecedented winter rainfall initiates large snow avalanche and mass movement cycle in New Zealand's Southern Alps/Kā Tiritiri o te Moana. *Geophysical Research Letters*, *50*, e2022GL102105. https://doi.org/10.1029/2022GL102105

Received 15 NOV 2022
Accepted 7 APR 2023

Author Contributions:

Conceptualization: Aubrey D. Miller, Pascal Sirguey, Yves Bühler
Data curation: Todd A. N. Redpath, Jono P. Conway
Formal analysis: Aubrey D. Miller, Todd A. N. Redpath, Pascal Sirguey, Perry Bartelt
Funding acquisition: Pascal Sirguey, Don Bogie, Nicolas J. Cullen

© 2023 The Authors.
This is an open access article under the terms of the Creative Commons Attribution-NonCommercial License, which permits use, distribution and reproduction in any medium, provided the original work is properly cited and is not used for commercial purposes.

Abstract An exceptional July 2022 winter storm brought 550 mm of precipitation to the Southern Alps of New Zealand. A series of alpine mass movements occurred during the storm, including a widespread snow avalanche cycle, debris flows, and erosion from rain runoff. We detail the sequence of events in the Kitchener avalanche path. Here, two large snow avalanches were followed by a debris flow. Substantial erosion of deposition and the underlying alluvial fan were induced by runoff from over 300 mm of rain falling after the first avalanche. The Kitchener path saw the largest avalanche since 1986, testing the utility of a diversion berm constructed for a 1:100-year event. Results from a unmanned aerial vehicle lidar survey and numerical modeling characterize the rain-on-snow hazard sequence. In particular, the rain-on-snow event occurred on a deep mid-winter snowpack, offering insights into future hazards posed by increasingly frequent extreme alpine precipitation.

Plain Language Summary Intense rain and snow in alpine regions can trigger snow avalanches, debris flows and other mass-movements, posing risks to people and infrastructure. This study documents an extreme hazard sequence triggered by a record-breaking winter rainstorm in the Southern Alps of New Zealand. A drone was used to map deposition from snow avalanches and a debris flow that ran along a diversion berm designed to protect Aoraki/Mount Cook Village from a 1:100-year avalanche. The mapping was used to calibrate avalanche modeling software that could replicate key characteristics of the snow avalanches and provide insight into flow dynamics. The documentation and results from the modeling can be used to plan for future hazards triggered by intense rain falling on a winter snowpack, which is particularly important in the face of a warming climate.

1. Introduction

Rain-on-snow events are often associated with downstream flooding (Marks et al., 1998) where precipitation duration and intensity and snowpack structure affect runoff rates (Würzer et al., 2016). Rain-on-snow events can also induce gravitational mass movements like avalanches and landslides, posing risks to people and infrastructure in alpine regions (Badoux et al., 2016; Dowling & Santi, 2013; Techel et al., 2016). Event documentation is necessary to gain knowledge of the mechanics involved in triggers and flow conditions and to build empirical evidence to underpin hazard probabilities (Bründl & Margreth, 2021). At the same time, dynamic models are useful for performing extreme-event scenarios in support of hazard planning and preparedness (Bühler et al., 2022). Model outputs (e.g., impact pressure, flow height) can help refine design specifications for structures that mitigate risks to people and infrastructure (Rudolf-Miklau et al., 2014). Detailed event documentation is necessary to calibrate dynamic models prior to hazard scenario-planning (Christen et al., 2010).

We document a sequence of mass movements (snow avalanches, debris flow, water runoff) in an avalanche path in the Southern Alps of New Zealand (NZ). Intense precipitation rates during the 18–19 July 2022 storm triggered a widespread avalanche cycle with avalanches reaching the valley floor in numerous paths (Figure 1b). This exceptional rain-on-snow induced avalanche cycle was followed by relatively small debris flows that overran snow avalanche deposition in several paths before both were eroded by rain runoff. We use the dynamic

19448007, 2023, 8, Downloaded from https://agupubs.onlinelibrary.wiley.com/doi/10.1029/2022GL102105 by Paul Scherrer Institut PSI, Wiley Online Library on [09/05/2023]. See the Terms and Conditions (https://onlinelibrary.wiley.com/terms-and-conditions) on Wiley Online Library for rules of use; OA articles are governed by the applicable Creative Commons License

Investigation: Aubrey D. Miller, Todd A. N. Redpath
Methodology: Aubrey D. Miller, Todd A. N. Redpath, Pascal Sirguey, Simon C. Cox, Yves Bühler
Project Administration: Aubrey D. Miller
Resources: Simon C. Cox, Don Bogie, Jono P. Conway
Software: Perry Bartelt, Yves Bühler
Supervision: Pascal Sirguey, Nicolas J. Cullen, Yves Bühler
Validation: Perry Bartelt
Visualization: Aubrey D. Miller, Todd A. N. Redpath
Writing – original draft: Aubrey D. Miller, Todd A. N. Redpath, Simon C. Cox, Don Bogie
Writing – review & editing: Aubrey D. Miller, Todd A. N. Redpath, Pascal Sirguey, Simon C. Cox, Perry Bartelt, Don Bogie, Jono P. Conway, Nicolas J. Cullen, Yves Bühler

model RApid Mass Movement Simulation (RAMMS) (Christen et al., 2010) to replicate the snow avalanche sequence that occurred in the Kitchener path (Figure 1c), based on meteorological observations, pre-event aerial and satellite photogrammetric mapping, a post-event unmanned aerial vehicle (UAV) survey, GNSS profiling of the runout zone and oblique photographs of the path.

While NZ's maritime climate generates rain-on-snow events to high elevations, the intensity and timing of this mid-winter storm falling on an above-average snowpack created conditions for an extreme wet avalanche cycle. Similar conditions have been documented in NZ (Fitzharris, 1976) and elsewhere (Decaulne & Sæmundsson, 2006; Eckerstorfer & Christiansen, 2011; Furdada et al., 1999). Characterizing such conditions will help better-anticipate future hazards, as wet avalanche activity may increase with a warming climate (Ballesteros-Cánovas et al., 2018; Castebrunet et al., 2014; Lazar & Williams, 2008) and rain-on-snow events may be more frequent at higher elevations (McCabe et al., 2007; Musselman et al., 2018).

2. Meteorology and Snowpack

Westerly airflow prevailed prior to the storm. North-westerly flow spread over the South Island over 17–19 July. ERA5 reanalysis data (Hersbach et al., 2020) indicate the advection of moisture across the Tasman Sea from the sub-tropics to the study region during the storm event (Figure S1 in Supporting Information S1). See Text S1 in Supporting Information S1 for detail on the synoptic situation before and during the event.

2.1. Weather Station Observations

Two automatic weather stations (AWS) provide meteorological and snowpack observations near the Kitchener path (see description in Hendrikx and Harper (2013)). Aoraki/Mount Cook Village AWS (hereafter MCV) is located at 730 m (elevations given as above sea level), 1 km south-east of the Kitchener path. Mueller Hut AWS (hereafter MH) is located at 1,818 m on the Sealy Range, *c.*1 km north of the Kitchener path release zone and 2.5 km from the main divide of the Southern Alps (Figure 1b).

The height of the snowpack (HS) at MH before the storm on 17 July (1.51 m) substantially exceeded the 2010–2022 mean HS of 0.96 m (standard deviation 0.41 m; Figure S2 in Supporting Information S1). HS at MH increased from 1.32 to 2.73 m during the storm. Concurrently, the shallow snowpack present at MCV (HS 0.33 m) was completely ablated. Early in the storm, MH snow temperature at 60 cm above ground level was −3.7°C. The MH snowpack warmed through the storm, warming rapidly between 01:00 and 04:00 on 18 July, reaching 0°C by 17:00, and stabilizing for the remainder of the storm (Figure 2a).

The freezing level (lapse rate of −0.0068°C m^{-1}, calculated from temperature differences between MH and MCV over 1 April to 31 July 2022) rose from the valley floor at MCV to ∼1,700 m on 16 July, before lowering slightly in the early hours of 17 July. Then, the freezing level rose episodically through 17-18 July, symptomatic of the successive arrival of increasingly warm airmasses. The freezing level exceeded the elevation of MH by 01:00 on 18 July, reaching a maximum elevation of *c.*2,100 m (Figure 2b).

Persistent rainfall at MCV steadily increased in intensity throughout the event. The 24-hr total to 09:00 on 19 July was 371 mm, with 547.8 mm recorded in the 72-hr total to 09:00 on 20 July. Maximum intensities, exceeding 20 mm hr^{-1}, occurred during the evening of 18 July, persisting into the early morning of 19 July. Rain rates of several mm hr^{-1} were observed at MH by the evening of 18 July, coincident with temperatures close to 2°C, indicating the occurrence of rain-on-snow at high elevations. Elevations below MH would have experienced rain-on-snow for all of 18 July, with elevations below 1,400 m likely affected from the onset of observed precipitation at MCV, resulting in a saturated isothermal snowpack.

Bulk snowpack density at MH, determined by dividing snow-pillow-measured snow water equivalent (SWE) (Figure 2f) by HS, was *c.*400 kg/m^{-3} prior to the storm. Between 12:00 on 18 July and 04:00 on 19 July, bulk density increased from 410 to 525 kg m^{-3}, coinciding with the period of heaviest rain at MCV. The occurrence of rain-on-snow and storm-maximum temperatures at MH over this time indicate likely contributions of both rain and snowmelt to an increase in free water within the snowpack.

2.2. Storm Total Precipitation in the Context of Historic Records

The 371 mm recorded on 19 July is a site record for 24-hr rainfall. Records at MCV begin on 1 April 2000 but can be extended with the historic record from Mt Cook, The Hermitage site (June 1928–March 2000; located

10.1029/2022GL102105

19448007, 2023, 8, Downloaded from https://agupubs.onlinelibrary.wiley.com/doi/10.1029/2022GL102105 by Paul Scherrer Institut PSI, Wiley Online Library on [08/05/2023]. See the Terms and Conditions (https://onlinelibrary.wiley.com/terms-and-conditions) on Wiley Online Library for rules of use; OA articles are governed by the applicable Creative Commons License

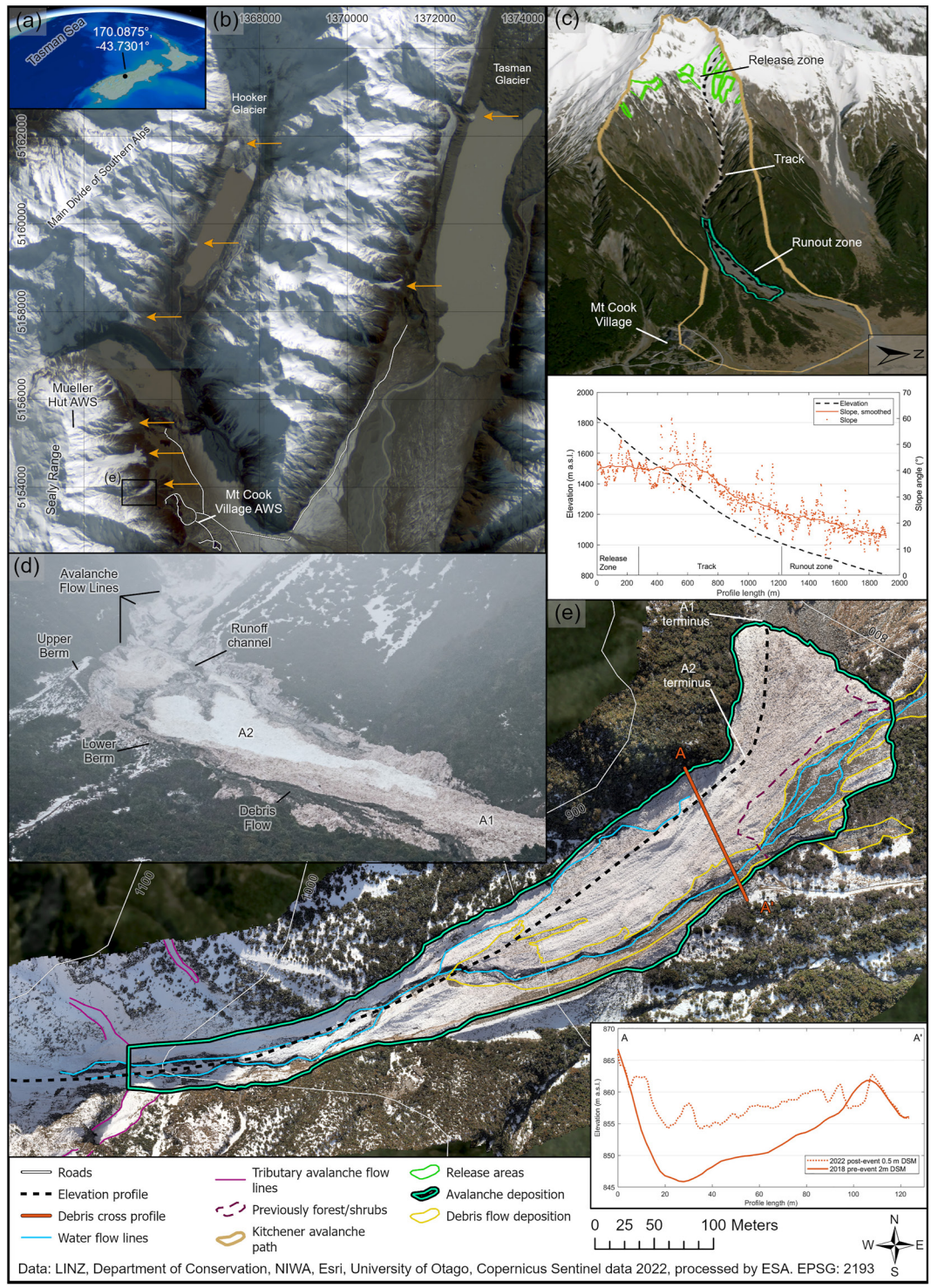

Figure 1. (a) Study site location. (b) Sentinel-2 image from 9 August 2022 depicting (orange arrows) some large avalanches from 18–19 July 2022 cycle. (c) Kitchener avalanche path and release areas used in numerical modeling with SkySat orthoimage from 22 October 2021 and elevation profile and slope gradient of path. (d) Oblique image of avalanche runout zone taken approximately 24 hr after the first snow avalanche (A1), courtesy of Taichiro Naka. (e) Runout zone of Kitchener path with orthoimage from unmanned aerial vehicle survey on 23 July 2022, with cross profile of runout zone.

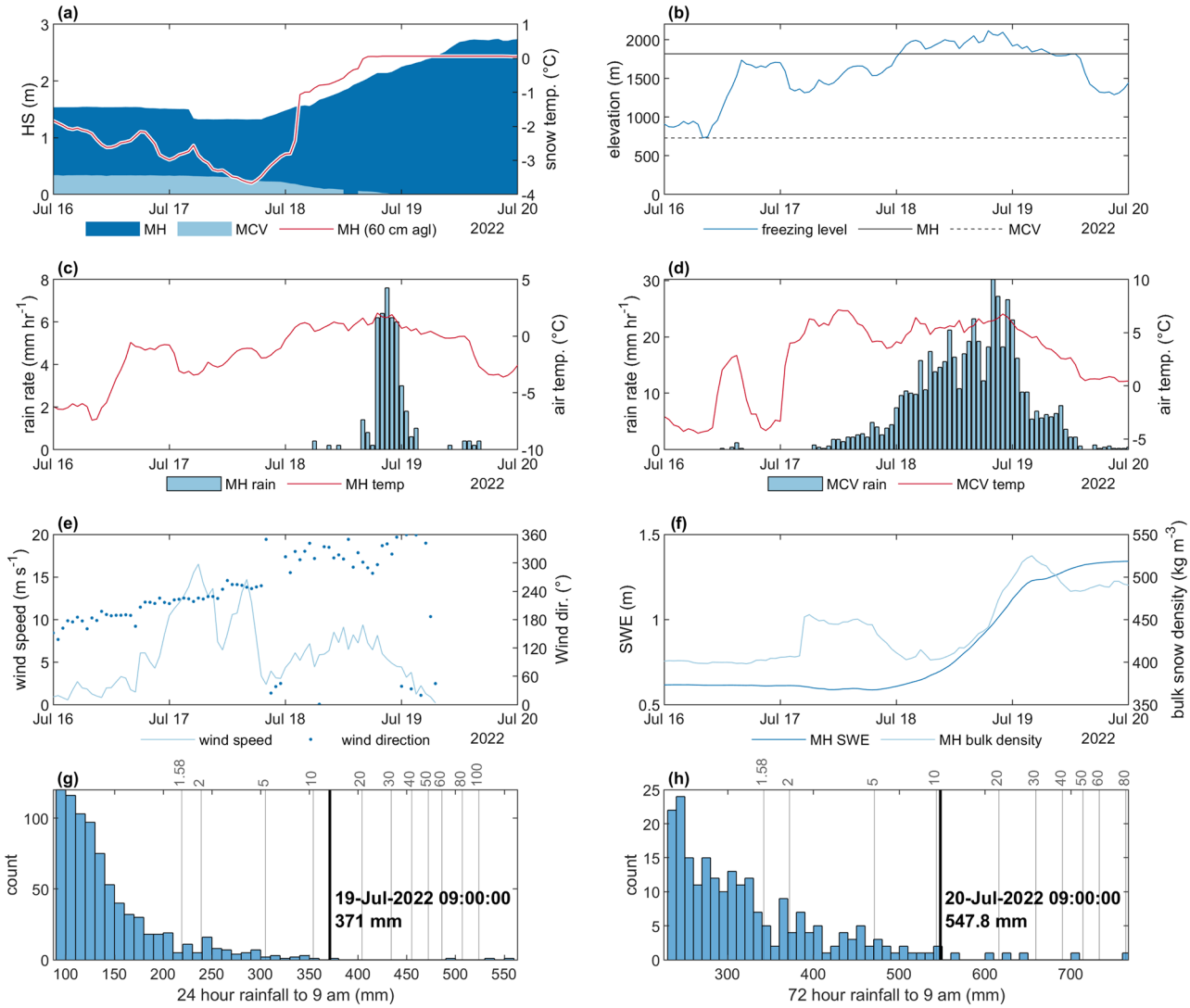

Figure 2. Mueller Hut (MH) and Aoraki/Mount Cook Village (MCV) weather station data showing (a) snow height (HS) and snow temperature from MH, (b) the freezing level determined by lapsing the observed MCV temperature, (c and d) hourly mean temperature and hourly total rainfall, (e) wind speed (hourly mean) and direction for MH (note data unavailable after 07:00 July 19), (f) snow water equivalent and bulk snow density for MH, (g) histogram of 24-hr and (h) 72-hr rainfall totals exceeding the 95th percentile from the extended MCV record, with HIRDS recurrence intervals (years) indicated by light gray vertical lines and July 2022 event noted with bold lines. HIRDS data retrieved from https://hirds.niwa.co.nz/.

within 250 m of MCV site). Within the combined 94-year record, this event ranks fourth for 24-hr rainfall and fourth for 72-hr rainfall (547.8 mm–20 July). Of 16 observed exceedances of 300 mm 24-hr rainfall, this was the first during a winter month (June, July or August) (Figures 2g and 2h). Observed rainfall depth exceeded the 10-year recurrence interval determined from the High Intensity Rainfall Design System (HIRDS; Carey-Smith et al., 2018) over both the 24- and 72-hr durations. While heavy precipitation occurs year-round at MCV, the probability of 24-hr rainfall events exceeding the 95th percentile (92 mm) is considerably dampened (<0.05) during winter months relative to the rest of the year. For the 99th percentile (172 mm) the contrast is even stronger (see Figure S3 in Supporting Information S1). This winter precipitation event is therefore unprecedented in the instrumental record at this location.

3. Avalanche Path Characteristics

The settlement of Aoraki/Mount Cook Village lies within 5 km of the main divide in Aoraki/Mount Cook National Park and is situated in the lower reach of the Kitchener avalanche path (Figure 1). Since 1965, nine

19448007, 2023, 8, Downloaded from https://agupubs.onlinelibrary.wiley.com/doi/10.1029/2022GL102105 by Paul Scherrer Institut PSI, Wiley Online Library on [09/05/2023]. See the Terms and Conditions (https://onlinelibrary.wiley.com/terms-and-conditions) on Wiley Online Library for rules of use; OA articles are governed by the applicable Creative Commons License

19448007, 2023, 8, Downloaded from https://agupubs.onlinelibrary.wiley.com/doi/10.1029/2022GL102105 by Paul Scherrer Institut PSI, Wiley Online Library on [09/05/2023]. See the Terms and Conditions (https://onlinelibrary.wiley.com/terms-and-conditions) on Wiley Online Library for rules of use; OA articles are governed by the applicable Creative Commons License

snow avalanches have been documented reaching the runout zone, the longest (July 1986) reaching 785 m (Jones & Bogie, 2018). There have been no documented avalanches reaching the village, however hazard assessments (Department of Conservation, 2009) suggested a risk of damage to the village by extreme avalanche events (>1:100-year). To mitigate this risk, a diversion berm was constructed in the runout zone to deflect the avalanche core away from the village. This structure, completed in 2018, had a design height up to 10 m and length of 305 m expected to provide protection from a 1:100-year dense core avalanche (Jones & Bogie, 2018).

The Kitchener path reaches as high as 2,000 m and includes a high cirque and low-angle bench. Below the bench is steep confined terrain that funnels avalanches into a main channel in the transition zone, or track, at 1,300 m before entering a widening runout zone at 1,000 m where the diversion berm begins (Figure 1c). Slope angles in the release zone range between 30 and 55° and are characterized by rough channelized terrain creating distinct potential release areas. The runout zone is relatively steep (mean slope angle 22°) until 800 m where slope gradients flatten. Shrubs and trees cover a portion of the lower runout zone, which also includes a popular walking track. No documented avalanches have destroyed forest since a 1957 flood and associated debris flow that affected large parts of the fan.

4. Event Sequence

4.1. Snow Avalanches

Evidence from oblique images of the path following the event suggests two main avalanches reached the runout zone (Figure 1d). The largest avalanche (A1) appears to have occurred first, resulting in a distinct lobate deposit of dirty snow and dispersed rocks and vegetation, crosscut and overlain by smaller deposits. Mapping of partly eroded crown/fracture lines, visible in oblique images after the event, indicates A1 started from distinct release areas (Figure 1c) between 1,500 and 1,900 m, however the precise release area extents are uncertain. Avalanche flows merged in the track before running into the runout zone. The avalanche entrained significant sediment and some vegetation, before destroying 8,800 m^2 of forest and shrubs in the runout zone. The total runout length was approximately 1,900 m, terminating at 802 m, with a mean slope angle of 30° along the profile (total runout/fahrböschung angle of 28°; Figure 1c). An avalanche forecaster in Aoraki/Mount Cook Village inferred the timing of the avalanche between 11:00 and 12:00 on 18 July.

Avalanche A1 splashed across the walls of the track in several places with flow lines and debris visible up to 30 m above the floor of the channel. When the avalanche reached the runout zone, it swept along the length of the diversion berm. Avalanche debris 1–2 m high was deposited at the top of the berm, with some snow splashing over the lower berm, however, the berm diverted the bulk of the avalanche as designed. Figure 1e shows a cross-profile of the debris from the post-event digital surface model (DSM), relative to the pre-event DSM. Erosion of the channel walls in the lower track led to the entrainment of sediment and vegetation, with evidence of erosion most pronounced along the southern wall of the channel as the avalanche entered the runout zone. Here, approximately 2,000 m^2 of vegetation and sediment 2–6 m deep were entrained into the avalanche.

A second snow avalanche (A2) was deposited across the top, and locally downcut into deposition from avalanche A1 (Figure 1d). Stopping approximately 120 m uphill from the toe of A1, the second avalanche deposited relatively clean white snow mainly down the true left side of the runout zone. The distinctively whiter color suggests it did not entrain as much sediment, possibly because the channel was filled with snow. It is inferred this event happened relatively soon after A1 from distinct release zones, possibly higher in elevation as the freezing level rose during the day of 18 July.

4.2. Debris Flow

Clay-to pebble-sized sediment lined channels cut into both avalanche deposits A1 and A2, linking to a series of dark sedimentary lobes deposited across the true right side of deposit A1. Fine sediment covered 15,200 m^2, running at least 450 m to the toe of the debris on the true right of deposit A1 and into the forest (Figure 1d). At some point, possibly as the result of initial damming of the river channel by the avalanche, a high-density debris flow appears to have developed. It may have burst out from beneath a dam of snow and ice or developed as runoff downcut into the freshly disturbed riverbed and eroded material from beneath the avalanche deposit. Either way, the continued precipitation and runoff into a catchment now disturbed by the presence of avalanche deposition,

19448007, 2023, 8, Downloaded from https://agupubs.onlinelibrary.wiley.com/doi/10.1029/2022GL102105 by Paul Scherrer Institut PSI, Wiley Online Library on [09/05/2023]. See the Terms and Conditions (https://onlinelibrary.wiley.com/terms-and-conditions) on Wiley Online Library for rules of use; OA articles are governed by the applicable Creative Commons License

appears to have generated several distinct secondary hazardous processes involving complex mixtures of water, rock, sediment and ice.

4.3. Water Runoff

Prior to the event sequence, the ephemeral Kitchener Creek generally flowed down the true left of the fan with water typically flowing underground below 800 m. After the event, water flow lines and channeling on the avalanche deposition were evident down the true left, however they do not reach the deposition toe. Flow lines and channeling were instead visible down the true right. The largest channel formed by the water runoff was *c.*3 m wide, incising through 3–4 m of deposition from the avalanche and debris flow, as well as *c.*1 m into the fan (Figures S5–S7 in Supporting Information S1). Sediment from the debris flow was carried and deposited beyond the snow avalanche debris. Precipitation rates between 10 and 30 mm hr^{-1} continued for 12 hr after A1 before rates dropped to between 2 and 10 mm hr^{-1} for a further 12 hr. More than 330 mm of precipitation was recorded in MCV over the 24 hr after the inferred timing of A1.

5. Event Mapping

5.1. Pre- and Post-Event Surveys

To estimate the volume of deposition from the mass movements in Kitchener path a pre-event DSM was differenced with a post-event DSM. The pre-event DSM was derived from a combination of aerial imagery (analog Leica RC30 camera, 153.73 mm lens, captured 2 November 2008) in release zone and track, and from satellite imagery (0.5 m Pléiades stereo-pair captured 29 March 2018) in runout zone, due to significant earthworks in the runout zone after the 2008 survey. Imagery was processed into a DSM using Ames Stereo Pipeline (ASP) v2.7 (Beyer et al., 2018; Shean et al., 2016) following the methods described in Eberhard et al. (2021).

A post-event survey was conducted 22–23 July 2022 to document the event and map the runout zone. A UAV (DJI Matrice 300 using real-time kinematic positioning with DJI L1 lidar sensor) mapped an area of 350,000 m^2 (density of 531 points m^2). The lidar point cloud was interpolated into a 0.5 m DSM using the point2dem tool in ASP. A second flight with a 35 mm ZenmuseP1 camera was used to generate a *c.*0.02 m orthomosaic (Figure 1e) used for mapping the deposition extent. A GNSS profile of the runout zone, post-processed from a dual-frequency, multi-constellation Trimble R10 logging at 1 Hz, was used to verify the pre- and post-event DSM heights. See Text S2 in Supporting Information S1 for DSM processing methods and uncertainties.

5.2. Volume Estimates

The total area of snow avalanche deposition mapped in the runout zone (below 1,020 m) was 61,000 m^2. An absolute difference of DEM (DoD) was calculated between the 2 m pre- and post-event DSMs ($DoD = DSM_{post} - DSM_{pre}$). Stable areas unaffected by the avalanche were used to assess the alignment between the DSMs, which found a mean elevation offset of 0.3 m (standard deviation 0.32 m; NMAD 0.31 m). The DoD was therefore adjusted by 0.3 m resulting in an adjusted volume of 175,860 ± 11,386 m^3 and mean deposition height of 2.7 m in the deposition area (Figure 3). Based on field observations of the debris flow deposition area, we estimate a 0.1 m average deposition depth, for a deposition volume of 1,520 m^3. The post-event DSM was collected five days after the event so contains modification of the deposition due to melting and erosion.

We leveraged the DoD to estimate erosion in the channel where all avalanche and debris flow deposition was removed (Figure S4 in Supporting Information S1). For areas where DoD <0—highlighting potential erosion of alluvial fan—the DoD revealed −2,260 ± 146 m^3 volume change. This may be the result of other geomorphic changes, in addition to erosion from this event. To assess the potential snow avalanche deposition eroded by water runoff, we assessed the area of the DoD adjacent to the main eroded channel through the avalanche and debris flow deposition and found a mean depth of 3.85 m (standard deviation 1.3 m). Applying this mean depth over the total area of the main eroded channel yields an eroded deposition volume estimate of −16,193 ± 745 m^3. Despite additional uncertainty around the extent to which the deposition was settled by subsequent rain and other runoff-related erosion of the deposition, we estimate a total avalanche deposition volume on the order of 200,000 m^3.

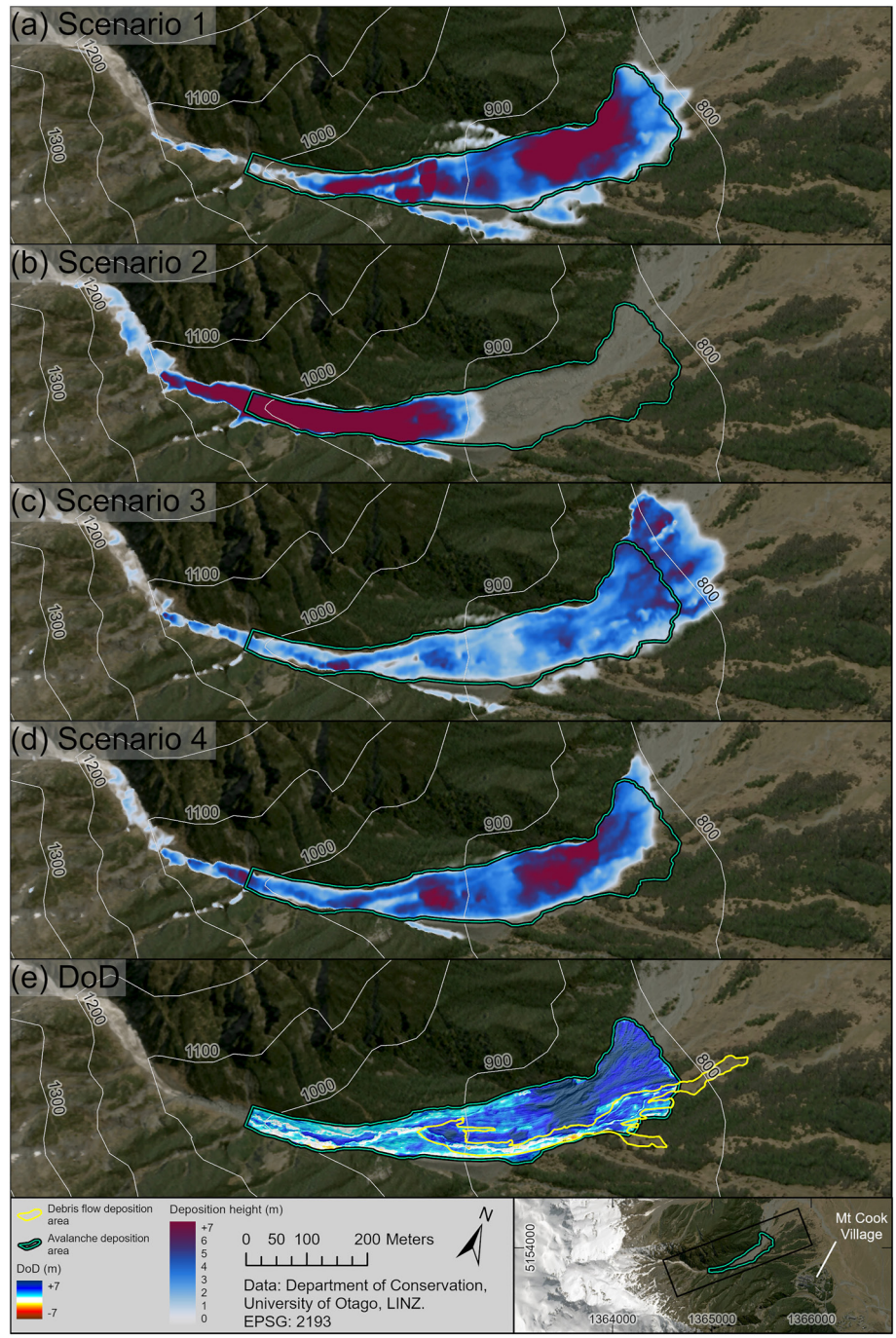

Figure 3. Avalanche scenarios from RApid Mass Movement Simulation simulations in panels (a–d) with a DEM of Difference (difference of DEM) between post-event 0.5 m digital surface model (DSM) and a pre-event 2018 2 m DSM in panel (e).

6. Snow Avalanche Modeling

6.1. Numerical Modeling

To better understand the avalanche dynamics, we used the extended version of RAMMS (Bartelt et al., 2016; Valero et al., 2016) to model the avalanche sequence. Four scenarios were simulated at 2 m resolution to find a set of parameters best matching the observed deposition pattern and runout length determined from the post-event UAV survey (Figure 3). A total release area of 60,070 m^2 (volume of 130,900 m^3) was comprised of nine individual

19448007, 2023, 8, Downloaded from https://agupubs.onlinelibrary.wiley.com/doi/10.1029/2022GL102105 by Paul Scherrer Institut PSI, Wiley Online Library on [08/05/2023]. See the Terms and Conditions (https://onlinelibrary.wiley.com/terms-and-conditions) on Wiley Online Library for rules of use; OA articles are governed by the applicable Creative Commons License

19448007, 2023, 8, Downloaded from https://agupubs.onlinelibrary.wiley.com/doi/10.1029/2022GL102105 by Paul Scherrer Institut PSI, Wiley Online Library on [09/05/2023]. See the Terms and Conditions (https://onlinelibrary.wiley.com/terms-and-conditions) on Wiley Online Library for rules of use; OA articles are governed by the applicable Creative Commons License

release areas based on oblique images where crown/fracture lines were partly visible (Figure 1c). Average release depths were between 1.25 and 2 m depending on elevation. See Text S3 in Supporting Information S1 for details on the uncertainties in the simulation initialization. To model avalanche A2 we delayed the release of three of these areas (total volume of 18,857 m^3), which ran over the erosion/deposition from A1 in the track and into the runout zone. A large release visible in the upper cirque was not included in the simulations because the debris deposited on a high bench.

We set the initial release conditions based on observations from MH weather station: snow density 400 kg m^{-3}, snow depth 1.85 m, snow temperature 0°C. The snow depth and temperature had an adjustment rate of 0.15 m 100 m^{-1}, 0.15°C 100 m^{-1}, respectively, to match observations from the MCV weather station. Initial simulations demonstrated the sensitivity to liquid water content (LWC) modeled in the snowpack at release, which was determined to be the most important driver of runout distance in this wet avalanche sequence. The LWC at release (LWC_0) was varied in the simulation scenarios.

6.2. RAMMS Scenarios

Scenario 1: We used friction and entrainment parameters informed by Miller et al. (2022). While not a rain-on-snow avalanche, the snowpack was warm (−0.8°C) at release with a similar snow depth profile within the path. The pertinent friction parameters were coulomb friction $\mu_0 = 0.55$, turbulent friction $\xi_0 = 1{,}500$ m s^{-2}, cohesion $N_0 = 200$ kPa, $LWC_0 = 0$ mm m^{-2}, generation of turbulent core energy $\alpha = 0.7$. It eroded 2.19× the release volume with a total deposition volume of 259,229 m^3 (average deposition depth of 4.5 m) located in the documented deposition area. The simulated avalanche ran approximately 55 m downhill of the true terminus. A2 stopped approximately 275 m uphill of the true terminus.

Scenario 2: We used friction parameters for wet avalanches ($\mu_0 = 0.55$, $\xi_0 = 500$ m s^{-2}, $N_0 = 500$ kPa, $\alpha = 0.5$, $LWC_0 = 0$ mm m^{-2}) used elsewhere (Bartelt et al., 2012, 2015; Valero et al., 2015, 2016, 2018). Once the LWC exceeded 100 mm m^{-2}, the friction μ transitioned to 0.12 (Valero et al., 2016). It eroded 1.48× the release volume with a total deposition volume of 148,369 m^3 (average deposition depth of 6.5 m). This simulation produced an avalanche that bulked up too much as the avalanche entered the runout zone, stopping 190 m uphill of the true terminus. A2 overran the deposition of A1 stopping just past the terminus of A1.

Scenario 3: We used the same wet avalanche friction parameters as in Scenario 2, except the release LWC_0 was set to 2 mm m^{-2}. It eroded 1.71× the release volume, with a total deposition volume of 157,601 m^3 (average deposition depth of 2.7 m). This resulted in an overly lubricated avalanche that flowed too far. A2 stopped approximately 175 m downhill of the true terminus.

Scenario 4: We used the same friction parameters as Scenarios 2 and 3, but with $LWC_0 = 1$ mm m^{-2}. It eroded 1.59× the release volume with a total deposition volume of 198,730 m^3 (average deposition depth of 3.6 m). This avalanche had the best fit with documented flow lines, deposition pattern and deposition volume. A2 came to stop within 10 m of the true terminus.

The Scenario 4 simulation adequately captured the flow characteristics through the track and runout zone based on flow-line evidence and areas of erosion/deposition. Results suggest the avalanche behaved as a typical large wet avalanche with moderate maximum velocities (40 m s^{-1} in the upper track, 10 m s^{-1} in top of runout zone). Modeled core pressures exceeded 300 kPa where considerable entrainment of sediment was observed. Modeled maximum core LWC exceeded 300 mm m^{-2}. The modeled total core mass was estimated as 140,999 t and total volume of 314,014 m^3.

While Scenario 4 best matched the observed deposition pattern, differences remain between the modeled and observed event. The modeled avalanche overran the true terminus by 50 m and did not impact the forest to the extent observed. This effect is likely due, in part, to a limitation of the depth-averaged modeling approach where the overtopping of deposition and localized friction conditions are challenging to model (Li et al., 2021). Also, the presence of vegetation in this portion of the fan increases the roughness in the DSM, decreasing runout length (Brožová et al., 2021).

7. Implications and Discussion

Low-frequency, large-magnitude events like the Kitchener event detailed here offer insight into the mass movement response to extreme rain falling on an above-average mid-winter snowpack. An extreme rain-on-snow event

19448007, 2023, 8, Downloaded from https://agupubs.onlinelibrary.wiley.com/doi/10.1029/2022GL102105 by Paul Scherrer Institut PSI, Wiley Online Library on [09/05/2023]. See the Terms and Conditions (https://onlinelibrary.wiley.com/terms-and-conditions) on Wiley Online Library for rules of use; OA articles are governed by the applicable Creative Commons License

in maritime Washington, USA induced a similar hazard sequence in January 2009 (Stimberis & Rubin, 2011). The Washington event had 285 mm of rain recorded over 52 hr, with significant snow avalanche activity after 15 hr (91 mm of rain), further slush avalanche activity after 152 mm, and a landslide after 185 mm. In comparison, the 2022 Kitchener event brought a total of 548 mm of rain to MCV over 72 hr, the majority falling within the first 52 hr (537 mm). By the end of the storm over 1.3 m of SWE was present at MH. The erosive mass movements documented in both events demonstrate the hazards posed by increasingly waterlogged snow as the storms progressed.

Kitchener avalanche A1 entrained significant sediment in the lower track and runout zone. Numerical modeling reveals the sensitivity to liquid water in the snowpack at release. A warm snowpack initialized with modest LWC matched observed avalanche flow characteristics. A slight increase in LWC generated significantly more free water when the avalanche was in motion, increasing the runout distance (Scenario 3). Had the avalanche occurred later in the storm cycle, increasing the amount of LWC in the snowpack, the runout distances could have been longer, likely destroying more forest and threatening a walking track. However, the estimated timing of the avalanche indicates that *c.*100 mm of rain in MCV was sufficient to release the main avalanche, and an increase of LWC from rain may not have been possible given the snowpack structure and state.

The diversion berm performed as designed to deflect the largest avalanche observed since 1986 away from Aoraki/Mount Cook Village. Overtopping of the berm would be likely with a larger avalanche, however, even with increased flowing volume, the bulk of the core would likely still be deflected (e.g., Scenario 1). Rain runoff did erode part of the lower berm, demonstrating the need to anticipate secondary hazards in the design of mitigative structures. Additional modeling scenarios (e.g., additional snow in path, existing debris in runout zone) would help anticipate future hazards in the path. Finally, a re-assessment of the diversion berm specification is needed, considering the extreme event detailed here, to help identify any necessary design changes to maintain the desired level of protection for the village.

This record-breaking mid-winter storm has implications for the hazard characteristics we can anticipate under future climate scenarios. Continued observational and modeling work is needed to understand the initiation of avalanches during significant rain-on-snow events. Assessing the importance of an increased frequency of moderate winter rainfall (e.g., >100 mm for Kitchener) and the emergence of new winter rainfall extremes (e.g., >300 mm for Kitchener), relative to the presence of an above average snowpack when these events occur, will support efforts to better understand the future evolution of hazard. At the same time, increased probabilities of rain-on-snow events occurring on mid-winter snowpacks in some regions may necessitate a review of existing hazard mitigation plans and defensive structures that may not have been designed for extreme rain-on-snow events.

Data Availability Statement

Meteorological data available from the National Institute of Water and Atmospheric Sciences (NIWA) CliFLo database (https://cliflo.niwa.co.nz/, registration required). Weather station snow data made available by NIWA under agreement with the University of Otago. ERA5 data available from Hersbach et al. (2023). The results of the UAV survey and event analysis are available from an interactive webmap (https://arcg.is/1aXm5f; Mountain Research Centre, 2022). Pléiades imagery used to generate the pre-event DSM was made available under licensed agreement © CNES (2018), and Airbus DS (2018), all rights reserved. Commercial uses forbidden. We used ASP v2.7 to for image processing and DSM generation (https://doi.org/10.5281/zenodo.3963341; Beyer et al., 2020). We used RAMMS::Extended for conducting the snow avalanche simulations (http://ramms.slf.ch/en/modules/extended.html; Christen et al., 2010; Bartelt et al., 2016; Valero et al., 2016).

Acknowledgments
We thank the following individuals and organizations: Taichiro Naka (Mountain Safety Council); George Loomes and Department of Conservation staff; Sam West (Interpine Innovation); Alan Jones, Mike Smallwood (Dynamic Avalanche Consulting); NIWA; NZ Aerial Mapping; Etienne Berthier (LEGOS/CNES). Support provided from University of Otago (Grant ORG-0118-0319), GNS Science (Grant GNS-DCF00043), MBIE (Grant UOOX1914). Contains information © CNES (2018), Distribution Airbus DS. Thanks to Editor Harihar Rajaram and three anonymous reviewers for constructive suggestions. Open access publishing facilitated by University of Otago, as part of the Wiley - University of Otago agreement via the Council of Australian University Librarians.

References

Badoux, A., Andres, N., Techel, F., & Hegg, C. (2016). Natural hazard fatalities in Switzerland from 1946 to 2015. *Natural Hazards and Earth System Sciences*, *16*(12), 2747–2768. https://doi.org/10.5194/nhess-16-2747-2016

Ballesteros-Cánovas, J. A., Trappmann, D., Madrigal-González, J., Eckert, N., & Stoffel, M. (2018). Climate warming enhances snow avalanche risk in the Western Himalayas. *Proceedings of the National Academy of Sciences*, *115*(13), 3410–3415. https://doi.org/10.1073/pnas.1716913115

Bartelt, P., Bühler, Y., Buser, O., Christen, M., & Meier, L. (2012). Modeling mass-dependent flow regime transitions to predict the stopping and depositional behavior of snow avalanches. *Journal of Geophysical Research*, *117*(F1), F01015. https://doi.org/10.1029/2010jf001957

Bartelt, P., Buser, O., Valero, C. V., & Bühler, Y. (2016). Configurational energy and the formation of mixed flowing/powder snow and ice avalanches. *Annals of Glaciology*, *57*(71), 179–188. https://doi.org/10.3189/2016aog71a464

Bartelt, P., Valero, C. V., Feistl, T., Christen, M., Bühler, Y., & Buser, O. (2015). Modelling cohesion in snow avalanche flow. *Journal of Glaciology*, *61*(229), 837–850. https://doi.org/10.3189/2015jog14j126

Beyer, R., Alexandrov, O., McMichael, S., Broxton, M., Lundy, M., Husmann, K., et al. (2020). NeoGeographyToolkit/StereoPipeline 2.7.0 [Code]. *Zenodo*. https://doi.org/10.5281/zenodo.3963341

Beyer, R. A., Alexandrov, O., & McMichael, S. (2018). The Ames Stereo Pipeline: NASA's open source software for deriving and processing terrain data. *Earth and Space Science*, *5*(9), 537–548. https://doi.org/10.1029/2018ea000409

Brožová, N., Baggio, T., D'Agostino, V., Bühler, Y., & Bebi, P. (2021). Multiscale analysis of surface roughness for the improvement of natural hazard modelling. *Natural Hazards and Earth System Sciences*. https://doi.org/10.5194/nhess-2021-85

Bründl, M., & Margreth, S. (2021). Chapter 9 - Integrative risk management: The example of snow avalanches. In W. Haeberli & C. Whiteman (Eds.), *Snow and ice-related hazards, risks, and disasters* (2nd ed., pp. 259–296). Elsevier. https://doi.org/10.1016/B978-0-12-817129-5.00002-0

Bühler, Y., Bebi, P., Christen, M., Margreth, S., Stoffel, L., Stoffel, A., et al. (2022). Automated avalanche hazard indication mapping on a statewide scale. *Natural Hazards and Earth System Sciences*, *22*(6), 1825–1843. https://doi.org/10.5194/nhess-22-1825-2022

Carey-Smith, T., Henderson, R., & Singh, S. (2018). High intensity rainfall design system, version 4. Technical report. Retrieved from https://niwa.co.nz/sites/niwa.co.nz/files/2018022CH_HIRDSv4_Final.pdf

Castebrunet, H., Eckert, N., Giraud, G., Durand, Y., & Morin, S. (2014). Projected changes of snow conditions and avalanche activity in a warming climate: The French Alps over the 2020–2050 and 2070–2100 periods. *The Cryosphere*, *8*(5), 1673–1697. https://doi.org/10.5194/tc-8-1673-2014

Christen, M., Kowalski, J., & Bartelt, P. (2010). RAMMS: Numerical simulation of dense snow avalanches in three-dimensional terrain. *Cold Regions Science and Technology*, *63*(1–2), 1–14. https://doi.org/10.1016/j.coldregions.2010.04.005

Decaulne, A., & Sæmundsson, Þ. (2006). Meteorological conditions during slush-flow release and their geomorphological impact in northwestern Iceland: A case study from the Bíldudalur valley. *Geografiska Annaler - Series A: Physical Geography*, *88*(3), 187–197. https://doi.org/10.1111/j.1468-0459.2006.00294.x

Department of Conservation. (2009). Section 3: Aoraki/Mount Cook Long Term Community Plan 2009–2019. Retrieved from https://www.doc.govt.nz/globalassets/documents/about-doc/role/policies-and-plans/national-park-management-plans/aoraki-ltcp-section3.pdf

Dowling, C. A., & Santi, P. M. (2013). Debris flows and their toll on human life: A global analysis of debris-flow fatalities from 1950 to 2011. *Natural Hazards*, *71*(1), 203–227. https://doi.org/10.1007/s11069-013-0907-4

Eberhard, L. A., Sirguey, P., Miller, A., Marty, M., Schindler, K., Stoffel, A., & Bühler, Y. (2021). Intercomparison of photogrammetric platforms for spatially continuous snow depth mapping. *The Cryosphere*, *15*(1), 69–94. https://doi.org/10.5194/tc-15-69-2021

Eckerstorfer, M., & Christiansen, H. H. (2011). Meteorology, topography and snowpack conditions causing two extreme mid-winter slush and wet slab avalanche periods in High Arctic Maritime Svalbard. *Permafrost and Periglacial Processes*, *23*(1), 15–25. https://doi.org/10.1002/ppp.734

Fitzharris, B. B. (1976). An avalanche event in the seasonal snow zone of the Mount Cook region, New Zealand. *New Zealand Journal of Geology and Geophysics*, *19*(4), 449–462. https://doi.org/10.1080/00288306.1976.10423539

Furdada, G., Martínez, P., Oller, P., & Vilaplana, J. M. (1999). Slushflows at El Port del Comte, northeast Spain. *Journal of Glaciology*, *45*(151), 555–558. https://doi.org/10.3189/s0022143000001428

Hendrikx, J., & Harper, A. (2013). Development of a national snow and ice monitoring network for New Zealand. *Journal of Hydrology (New Zealand)*, *52*, 83–95. Retrieved from https://www.jstor.org/stable/43945047

Hersbach, H., Bell, B., Berrisford, P., Biavati, G., Horányi, A., Muñoz Sabater, J., et al. (2023). ERA5 hourly data on single levels from 1940 to present. Copernicus Climate Change Service (C3S) Climate Data Store (CDS). https://doi.org/10.24381/cds.adbb2d47

Hersbach, H., Bell, B., Berrisford, P., Hirahara, S., Horányi, A., Muñoz-Sabater, J., et al. (2020). The ERA5 global reanalysis. *Quarterly Journal of the Royal Meteorological Society*, *146*(730), 1999–2049. https://doi.org/10.1002/qj.3803

Jones, A., & Bogie, D. (2018). Design and construction of an avalanche deflection berm, Mount Kitchener Avalanche Path, Aoraki Mount Cook National Park, New Zealand. In *International Snow Science Workshop Proceedings 2018* (pp. 197–201). Retrieved from https://arc.lib.montana.edu/snow-science/objects/ISSW2018_P02.18.pdf

Lazar, B., & Williams, M. (2008). Climate change in western ski areas: Potential changes in the timing of wet avalanches and snow quality for the Aspen ski area in the years 2030 and 2100. *Cold Regions Science and Technology*, *51*(2–3), 219–228. https://doi.org/10.1016/j.coldregions.2007.03.015

Li, X., Sovilla, B., Jiang, C., & Gaume, J. (2021). Three-dimensional and real-scale modeling of flow regimes in dense snow avalanches. *Landslides*, *18*(10), 3393–3406. https://doi.org/10.1007/s10346-021-01692-8

Marks, D., Kimball, J., Tingey, D., & Link, T. (1998). The sensitivity of snowmelt processes to climate conditions and forest cover during rain-on-snow: A case study of the 1996 Pacific Northwest flood. In *Hydrological processes* (Vol. 12, pp. 1569–1587).

McCabe, G. J., Clark, M. P., & Hay, L. E. (2007). Rain-on-snow events in the western United States. *Bulletin of the American Meteorological Society*, *88*(3), 319–328. https://doi.org/10.1175/bams-88-3-319

Miller, A., Sirguey, P., Morris, S., Bartelt, P., Cullen, N., Redpath, T., et al. (2022). The impact of terrain model source and resolution on snow avalanche modeling. *Natural Hazards and Earth System Sciences*, *22*(8), 2673–2701. https://doi.org/10.5194/nhess-22-2673-2022

Mountain Research Centre. (2022). Interactive web map of study results [Dataset]. ArcGIS Online. Retrieved from https://arcg.is/1aXm5f

Musselman, K. N., Lehner, F., Ikeda, K., Clark, M. P., Prein, A. F., Liu, C., et al. (2018). Projected increases and shifts in rain-on-snow flood risk over western North America. *Nature Climate Change*, *8*(9), 808–812. https://doi.org/10.1038/s41558-018-0236-4

Rudolf-Miklau, F., Skolaut, C., & Sauermoser, S. (2014). Avalanche hazard assessment and planning of protection measures. In *The Technical Avalanche Protection Handbook* (pp. 91–126). John Wiley & Sons, Ltd. https://doi.org/10.1002/9783433603840.ch04

Shean, D. E., Alexandrov, O., Moratto, Z. M., Smith, B. E., Joughin, I. R., Porter, C., & Morin, P. (2016). An automated, open-source pipeline for mass production of digital elevation models (DEMs) from very-high-resolution commercial stereo satellite imagery. *ISPRS Journal of Photogrammetry and Remote Sensing*, *116*, 101–117. https://doi.org/10.1016/j.isprsjprs.2016.03.012

Stimberis, J., & Rubin, C. M. (2011). Glide avalanche response to an extreme rain-on-snow event, Snoqualmie Pass, Washington, USA. *Journal of Glaciology*, *57*(203), 468–474. https://doi.org/10.3189/002214311796905686

Techel, F., Jarry, F., Kronthaler, G., Mitterer, S., Nairz, P., Pavšek, M., et al. (2016). Avalanche fatalities in the European Alps: Long-term trends and statistics. *Geographica Helvetica*, *71*(2), 147–159. https://doi.org/10.5194/gh-71-147-2016

Valero, C. V., Jones, K. W., Bühler, Y., & Bartelt, P. (2015). Release temperature, snow-cover entrainment and the thermal flow regime of snow avalanches. *Journal of Glaciology*, *61*(225), 173–184. https://doi.org/10.3189/2015jog14j117

Valero, C. V., Wever, N., Bühler, Y., Stoffel, L., Margreth, S., & Bartelt, P. (2016). Modelling wet snow avalanche runout to assess road safety at a high-altitude mine in the central Andes. *Natural Hazards and Earth System Sciences*, *16*(11), 2303–2323. https://doi.org/10.5194/nhess-16-2303-2016

19448007, 2023, 8, Downloaded from https://agupubs.onlinelibrary.wiley.com/doi/10.1029/2022GL102105 by Paul Scherrer Institut PSI, Wiley Online Library on [09/05/2023]. See the Terms and Conditions (https://onlinelibrary.wiley.com/terms-and-conditions) on Wiley Online Library for rules of use; OA articles are governed by the applicable Creative Commons License

Valero, C. V., Wever, N., Christen, M., & Bartelt, P. (2018). Modeling the influence of snow cover temperature and water content on wet-snow avalanche runout. *Natural Hazards and Earth System Sciences*, *18*(3), 869–887. https://doi.org/10.5194/nhess-18-869-2018

Würzer, S., Jonas, T., Wever, N., & Lehning, M. (2016). Influence of initial snowpack properties on runoff formation during rain-on-snow events. *Journal of Hydrometeorology*, *17*(6), 1801–1815. https://doi.org/10.1175/jhm-d-15-0181.1

References From the Supporting Information

d'Angelo, P. (2016). Improving semi-global matching: Cost aggregation and confidence measure. *International Archives of the Photogrammetry, Remote Sensing and Spatial Information Sciences*, *41*, 299–304. https://doi.org/10.5194/isprs-archives-xli-b1-299-2016

DJI. (2021a). Zenmuse P1 user manual, v1.2. Retrieved from https://dl.djicdn.com/downloads/Zenmuse_P1/20210510/Zenmuse_P1%20_User%20Manual_EN_v1.2_3.pdf

DJI. (2021b). Zenmuse L1 user manual, v1.2. Retrieved from https://dl.djicdn.com/downloads/Zenmuse_L1/20220119UM/Zenmuse_L1%20_User%20Manual_EN_v1.2-1.pdf

Hirschmuller, H. (2008). Stereo processing by semiglobal matching and mutual information. *IEEE Transactions on Pattern Analysis and Machine Intelligence*, *30*(2), 328–341. https://doi.org/10.1109/tpami.2007.1166

Macara, G. R. (2016). *The Climate and Weather of Canterbury*, *NIWA Science and Technology Series Number 68* (2nd ed., p. 44). National Institute of Water and Atmospheric Research (NIWA). Retrieved from https://niwa.co.nz/our-science/climate/publications/regional-climatologies/canterbury

Prince, H. D., Cullen, N. J., Gibson, P. B., Conway, J., & Kingston, D. G. (2021). A climatology of atmospheric rivers in New Zealand. *Journal of Climate*, *34*(11), 4383–4402. https://doi.org/10.1175/JCLI-D-20-0664.1

Sirguey, P., & Cullen, N. (2014). A very high resolution DEM of Kilimanjaro via photogrammetry of GeoEye-1 images (KILISoSDEM2012). *New Zealand Surveyor*, *303*, 19–215.

19448007, 2023, 8, Downloaded from https://agupubs.onlinelibrary.wiley.com/doi/10.1029/2022GL102105 by Paul Scherrer Institut PSI, Wiley Online Library on [08/05/2023]. See the Terms and Conditions (https://onlinelibrary.wiley.com/terms-and-conditions) on Wiley Online Library for rules of use; OA articles are governed by the applicable Creative Commons License